Large coherence of spanwise velocity in turbulent boundary layers

C. M. de Silva
Dept. of Mech. Eng.
The University of Melbourne
Victoria 3010, Australia
desilvac@unimelb.edu.au

Kevin
Dept. of Mech. Eng.
The University of Melbourne
Victoria 3010, Australia
kevin.kevin@unimelb.edu.au

R. Baidya
Dept. of Mech. Eng.
The University of Melbourne
Victoria 3010, Australia
baidyar@unimelb.edu.au

N. Hutchins
Dept. of Mech. Eng.
The University of Melbourne
Victoria 3010, Australia
nhu@unimelb.edu.au

I. Marusic
Dept. of Mech. Eng.
The University of Melbourne
Victoria 3010, Australia
imarusic@unimelb.edu.au

Abstract

This study investigates the spatial signature of spanwise velocity coherence in turbulent boundary layers. A series of unique large field-of-view multi-camera particle image velocimetry (PIV) experiments are conducted in a planar arrangement at a friction Reynolds number of $Re_\tau \approx 2600$. The experiments are configured to capture streamwise/spanwise slices of a turbulent boundary layer in both the logarithmic and wake regions. Consistent with numerical observation of Sillero *et al.* (2014), we observe a pronounced oblique pattern of spanwise velocity coherence with an orientation dependant on the sign of the spanwise velocity. This behaviour is sufficiently strong to be distinguished in the instantaneous flow fields and mostly obvious in the outer most part of the layer. Additionally, we observe that this oblique arrangement dictates the alignment of the intermittent turbulent bulges, which leads to a pronounced impact on the geometry of the turbulent/non-turbulent interface. Finally, we test whether a boundary layer constructed using a model based on the attached eddy hypothesis can produce similar behaviour for the coherence of spanwise velocity. Comparisons between the model and experimental velocity fields reveal some degree of similarity with both exhibiting coherent regions of spanwise velocity that are arranged diagonally.

Introduction

The structural nature of turbulent boundary layers has been the subject of many investigations. Recent summaries on these structural features are discussed by Marusic & Adrian (2012) and Herpin *et al.* (2013). Over the last decade the presence of large-scale motions on the order of the boundary layer thickness have received considerable interest. However, a large number of these studies have focused on the coherence of the streamwise velocity component, and subsequently coherent regions in the other velocity components remain largely unexplored. This is particularity true for the spanwise velocity component.

One distinct feature reported recently for the spanwise velocity is the existence of large coherent regions in the outer region of turbulent boundary layers (Sillero *et al.*, 2014). These features are best described with reference to figure 1, which shows a representative example from the present PIV experiment. The colour contours correspond to spanwise velocity fluctuations, v, which are shown on a streamwise/spanwise plane at a wall-normal height of $z/\delta \approx 1$. Here, boundary layer thickness δ corresponds to wall-normal location, where the mean velocity is 99% of the free-stream velocity. Qualitatively, it is evident that the δ-scaled coherent regions of spanwise velocity in the outer region of a boundary layer are oriented in an oblique arrangement. Specifically, regions of positive and negative $\widetilde{V}$ appear to be counter-oriented at oblique angles, and have characteristic lengths in excess of $O(\delta)$ in both the spanwise and streamwise directions. Therefore, although these features are easily distinguishable when the FOV is very large, most prior PIV experiments have insufficient spatial extents to capture these large-scale motions. Moreover, the few experiments that have large spatial extents, particularly on streamwise/spanwise planes generally focus on the logarithmic region of boundary layers, where the largest coherent regions of streamwise velocity appear to reside (Westerweel *et al.*, 2013). The PIV experiments with very large spatial extents targeted at the logarithmic and wake regions presented herein offer a promising approach to carefully examine these large-scale motions. However, the approach is not without its own difficulties; some structures are known to commonly persist for streamwise distances exceeding 10δ (Hutchins & Marusic, 2007). Capturing the full extent of these features with PIV requires multiple cameras to obtain sufficient spatial resolution over a large spatial domain (de Silva *et al.*, 2014).

Encouraged by recent observations from numerical databases (Sillero *et al.*, 2014), this study aims to understand the mechanisms that may explain the large-scale oblique patterns of $\widetilde{V}$ in turbulent boundary layers. We begin with a description of the PIV experiments. Thereafter, a discussion on the structural arrangement of $\widetilde{V}$ is presented as a function of wall-normal location and Reynolds number.

Throughout this work, the coordinate system x, y and z refers to the streamwise, spanwise and wall-normal directions, respectively. Corresponding instantaneous streamwise, spanwise and wall-normal velocities are represented by $\widetilde{U}$, $\widetilde{V}$ and $\widetilde{W}$, respectively. Overbars and $\langle\rangle$ denote average quantities and the superscript + refers to normalisation by inner scales. For example, we use $\widetilde{U}^+ = \widetilde{U}/U_\tau$ for velocity, where U_τ is the friction velocity.

Description of experiments

The experiments are performed in the High Reynolds Number Boundary Layer Wind Tunnel (HRNBLWT) at the University of Melbourne. The tunnel consists of a large development length of approximately 27m, offering the capability of achieving high Reynolds numbers at relatively low free-stream velocities. This provides a uniquely thick boundary layer at Re_τ up to 25000, re-

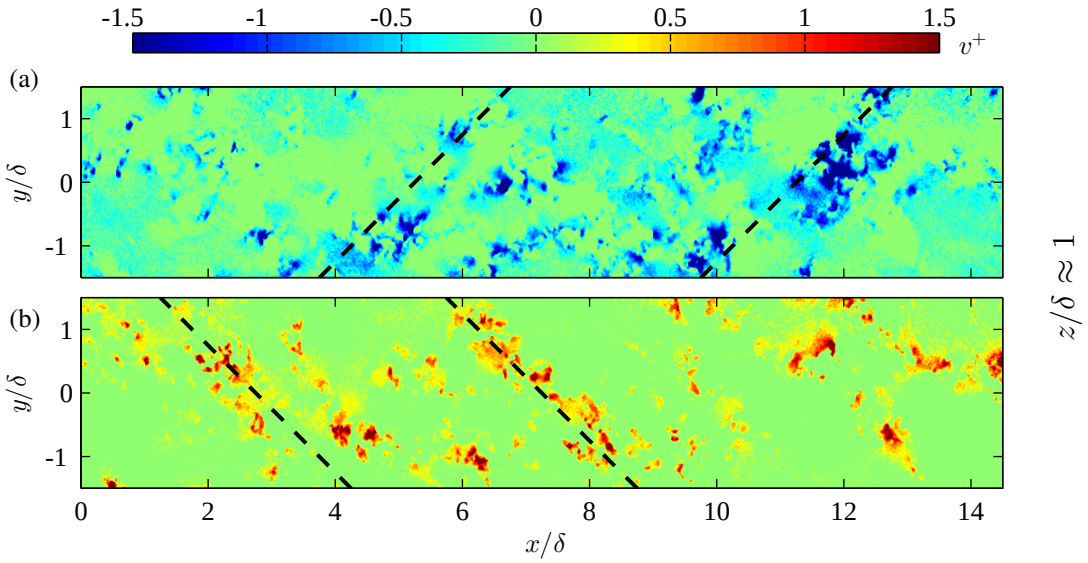

Figure 1: Colour contours of spanwise velocity fluctuations, v of a turbulent boundary layer. Results are presented on a streamwise/spanwise plane at $z/\delta \approx 1$ at $Re_\tau \approx 2600$. (a) and (b) shows the same flow field decomposed by the sign of v, where (a) shows only contours where $v < 0$ and (b) when $v > 0$. The black dashed lines correspond to ±45°.

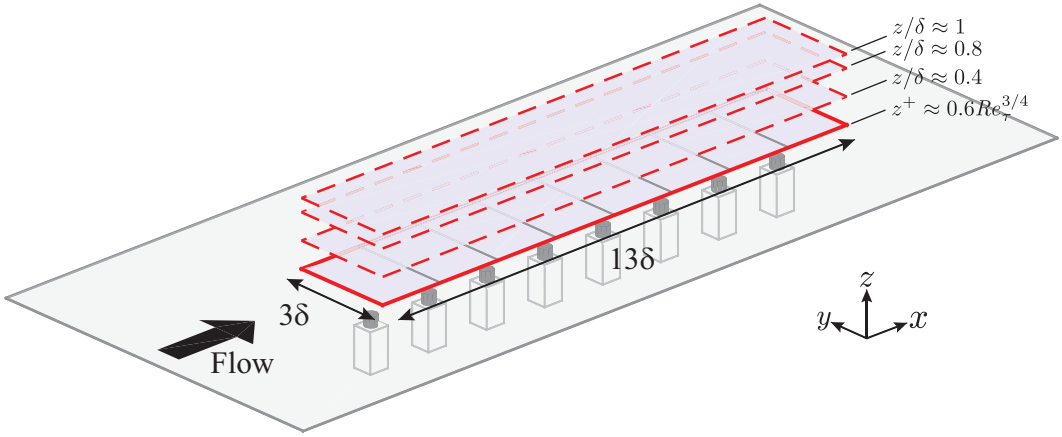

Figure 2: Experimental setup used to conduct large field of view planar PIV experiments in the HRNBLWT to capture a streamwise/spanwise plane. The red solid line corresponds to the combined field of view captured from the multi-camera imaging system at the geometric centre of the log-region ($z \approx 0.6Re_\tau^{3/4}$), and the red dashed lines correspond to the higher wall-normal locations ($z/\delta \approx 0.4$, 0.8 and 1) captured.

sulting in a larger measurable viscous length scale (hence less acute spatial resolution issues) (Nickels *et al.*, 2005). Unlike prior PIV campaigns in the HRNBLWT (de Silva *et al.*, 2014), which are tailored to achieve the highest *Re* possible from the facility, the present experiments are configured to obtain snapshots of very large scale structures of $O(10\delta)$ with sufficient fidelity. Accordingly, the experiments are conducted at the upstream end of the test section ($x \approx 5$ m), where the boundary layer is thinner (with a thickness of $\delta \approx 90$ mm). We note that δ is still large relative to many boundary layer facilities, but small compared to that achievable further downstream in the HRNBLWT. In order to capture relatively well-resolved velocity fields with a streamwise extent of $O(10\delta)$, the field of view (FOV) is constructed by stitching eight high-resolution 14 bit PCO 4000 PIV cameras. The cameras are arranged (see figure 2) to quantify velocity fields on a streamwise/spanwise – hereafter referred to as the *xy* plane. The red solid and dashed lines in figure 2 show the combined field of view at different wall-normal locations from the eight cameras, which spans approximately 13δ in the streamwise direction and 3δ in the spanwise direction. Each camera has a resolution of 4008×2672 pixels, therefore the pixel size is ~65µm/pixel, respectively. Measurements are acquired at 10 m/s and the *xy* planes are captured at four different wall-normal locations spanning the geometric centre of the logarithmic and wake regions of the flow. A summary of the flow parameters of the experimental databases is provided in table 1.

To maintain a constant z/δ across the long streamwise domain of the *xy* plane, the laser sheet is tilted at a very shallow angle to accommodate the growth rate of the boundary layer (which closely approximates to a linear growth over this streamwise extent). Seeding particles are injected in close proximity to the blower fan, which is then allowed to circulate throughout the entire laboratory to obtain a homogeneous seeding density across the test section.

Wall-normal location	U_∞ (m/s)	Re_τ	ν/U_τ (μm)	δ (m)	PIV images
$z^+ \approx 0.6Re_\tau^{3/4}$	10	2500	42	0.09	3000
$z/\delta \approx 0.4$					1000
$z/\delta \approx 0.8$					3000
$z/\delta \approx 1$					1000

Table 1: Flow parameters of experimental data. The friction velocity U_τ is computed at the middle of the FOV.

Laser sheet thickness	$\approx$ 1mm or $\approx 24^+$
Particle size	$\approx 1-2$ μm
Seeding	Polyamide particles
Flow medium	Air
Field of view	$\approx 1.3\text{m} \times 0.25\text{m}$
Depth of field	$\approx$ 5mm
Optical magnification	$\approx 65\mu\text{m/pixel}$
Interrogation window size	32×32 pixels or $\approx 50^+$
Vector Overlap	50%
Vectors per image	$\approx 5 \times 10^5$

Table 2: Experimental and processing parameters for the PIV experiments

Particle illumination is provided by a Spectra Physics PIV400 Nd-YAG double pulse laser using a typical PIV optical configuration. However, to ensure adequate illumination levels across the large spatial extent of O(m), the laser sheet is projected upstream through the working section. For the present work the laser sheet thickness is quantified by the method outlined by Grayson *et al.* (2016). The image pairs are processed using an in-house PIV package developed at the University of Melbourne (de Silva *et al.*, 2014). Key processing parameters including the final interrogation window size and properties of the imaging system are summarised in table 2.

Validation

In order to quantify the quality of the databases from the present work, figure 3 presents mean velocity and turbulence intensity profiles. The ▲ symbols correspond to results from PIV database from the present work, while the solid red (—) lines correspond to a recent direct numerical simulation (DNS) database Sillero *et al.* (2013). Because the PIV and DNS databases are at comparable Re, they provide an appropriate means to benchmark the quality of the experiments, isolating any experimental uncertainties which are not present in DNS.

The results show good agreement for the mean flow ($\overline{U}/U_\infty$) between the PIV databases at all four wall locations to the DNS databases. Similarly, the turbulence intensities ($\overline{u^2}/U_\infty^2$ and $\overline{v^2}/U_\infty^2$) also exhibit good agreement with some degree of spatial attenuation closer to the wall, which is to be expected from PIV measurements. To explore the influence of spatial averaging further, following Lee *et al.* (2016) we spatially box filter the DNS database at matched

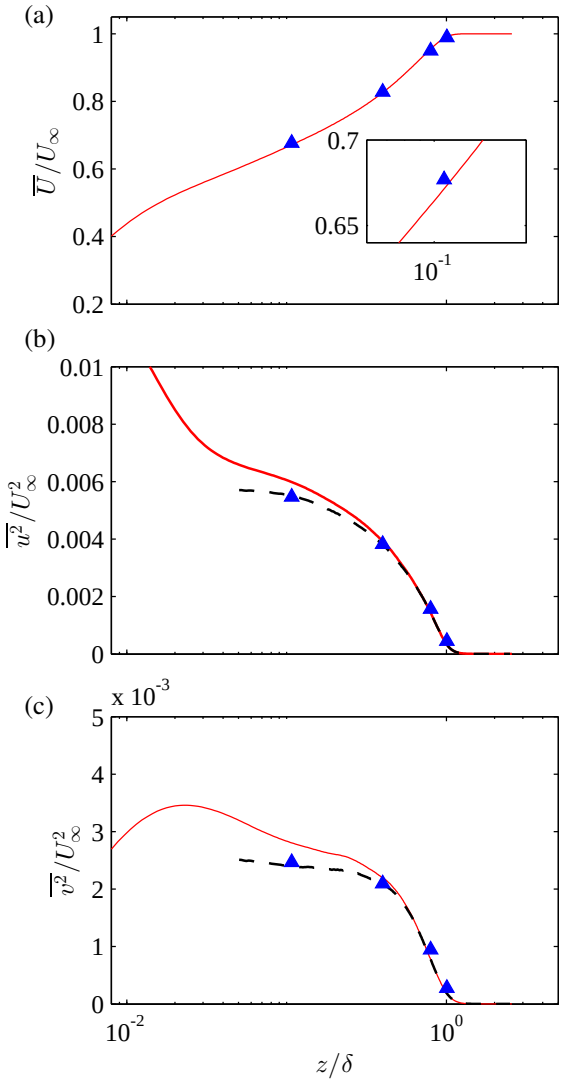

Figure 3: Comparison of flow statistics: (a) mean streamwise velocity U/U_∞, (b) streamwise turbulence intensity $\overline{u^2}/U_\infty^2$ and (c) spanwise turbulence intensity $\overline{v^2}/U_\infty^2$. The ▲ symbols correspond to results from PIV database at different wall normal heights, and the solid red lines correspond to a recent DNS database at $Re_\tau \approx 2500$ (Sillero *et al.*, 2013). The dashed black line in (b-c) corresponds to statistics from the $Re_\tau = 2500$ DNS database filtered to match the spatial resolution of the PIV measurement.

spatial resolution to the PIV database. We note that box filter size is chosen to match the interrogation window size and laser sheet thickness. The results are shown by the black dashed (−−) lines in figure 3(b-c), which corresponds to the turbulence intensity levels obtained from the box-filtered DNS velocity fields. Good agreement is observed between the PIV and filtered DNS statistics, confirming that the discrepancy observed in the near-wall region is largely due to spatial attenuation from the PIV measurements. Results presented in figure 3 are normalised by U_∞ however, normalisation by U_τ also provides similar findings (not reproduced here for brevity).

As a final note, since we employ a low magnification level, particle diameters are $\approx 1-2$ pixels. This size is less than that recommended for PIV experiments (Adrian & Westerweel, 2011), and therefore can lead to pixel-locking of the velocity fields (Wester-

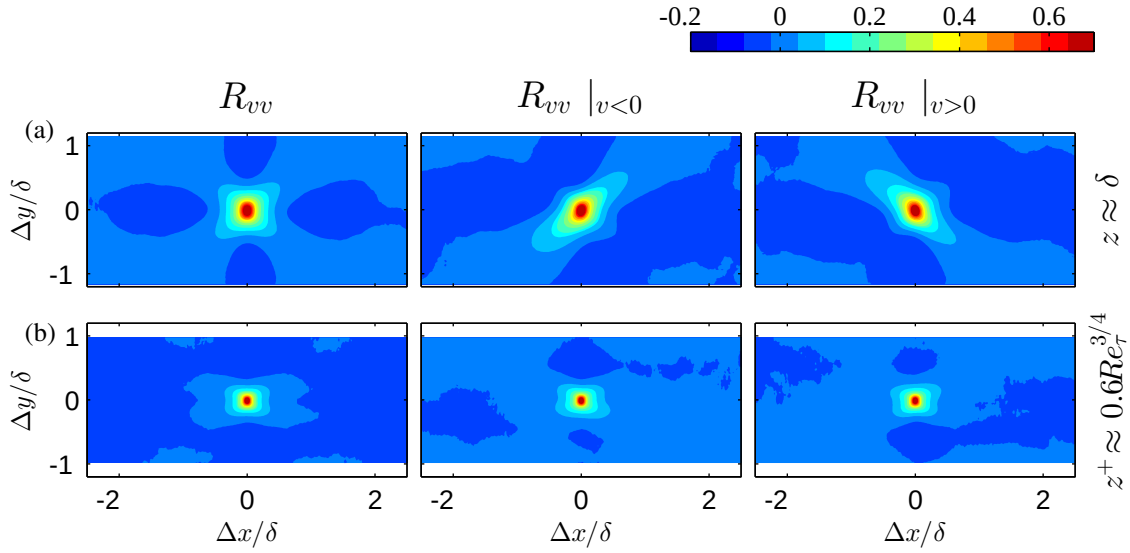

Figure 4: Wall-parallel slices of the correlation function of the spanwise velocity, R_{vv}. Rows present results at different wall-normal locations: (a) $z \approx \delta$, (b) $z^+ \approx 0.6Re_\tau^{3/4}$. Left columns presents the unconditional R_{vv}, and the middle and right columns present R_{vv} when $v < 0$ and $v > 0$, respectively.

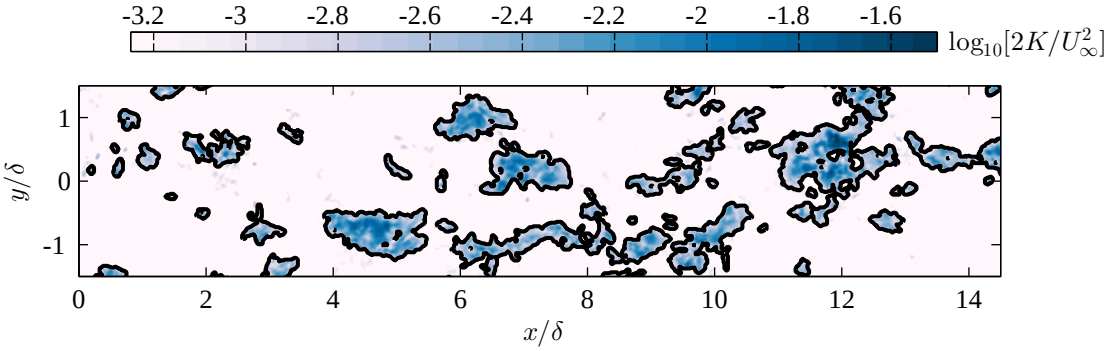

Figure 5: Instantaneous colour contours of kinetic energy deficit, K, on a logarithmic scale. Results are presented on a xy plane at $z/\delta \approx 1$ for the same velocity field shown in figure 1. The solid black line indicates the location of the TNTI computed as an iso-kinetic energy surface using a threshold of $K_0 = 10^{-3}\left(\frac{1}{2}U_\infty^2\right)$.

weel, 1997). To minimise this shortcoming, a Gaussian kernel filter is applied to the raw images (Adrian & Westerweel, 2011). Additionally, the window deformation technique used here during vector evaluation is also known to further reduce the influence of pixel-locking (Scarano, 2001). To ensure a negligible degree of pixel locking is present, p.d.f's of $\widetilde{U}$ are examined from each dataset (not reproduced here). These statistics verified that the bias towards integer pixel displacements is minimal.

Results

To quantify the strong persistent structural arrangement of coherent regions of spanwise velocity, figure 4 presents two-point correlation function of the spanwise velocity, R_{vv}, at two representative wall-normal locations. The left column correspond to the unconditional normalised autocorrelation, $R_{vv}(\mathbf{x}, \mathbf{x}') = \overline{v(\mathbf{x}).v(\mathbf{x}')}/\sigma_v^2$, where $\mathbf{x}'$ is the reference point and $\mathbf{x}$ is the moving point. Normalisation here is by the corresponding standard deviation. In similar fashion, the middle and right columns of figure 4 present the autocorrelation, R_{vv}, conditioned on the sign of the spanwise velocity fluctuations following

$$R_{vv}(\mathbf{r}, \mathbf{r}')|_{v(\mathbf{r}')<0} = \frac{\overline{v(\mathbf{r}).v(\mathbf{r}')}|_{v(\mathbf{r}')<0}}{\sigma_v^2|_{v(\mathbf{r}')<0}} \tag{1}$$

and

$$R_{vv}(\mathbf{r}, \mathbf{r}')|_{v(\mathbf{r}')>0} = \frac{\overline{v(\mathbf{r}).v(\mathbf{r}')}|_{v(\mathbf{r}')>0}}{\sigma_v^2|_{v(\mathbf{r}')>0}}. \tag{2}$$

The results computed in the edge of boundary layer (figure 4a) clearly show that regions of positive and negative v appear to be statistically counter-oriented at oblique angles, in agreement with the instantaneous inspections (see figure 1). These findings also reaffirm prior observations from numerical databases (Sillero *et al.*, 2014). Very similar correlation maps to those produced at $z/\delta \approx 1$ are also observed at $z/\delta \approx 0.8$ (not plotted here). Meanwhile, relatively closer to the wall (figure 4b), R_{vv} appears not to exhibit such

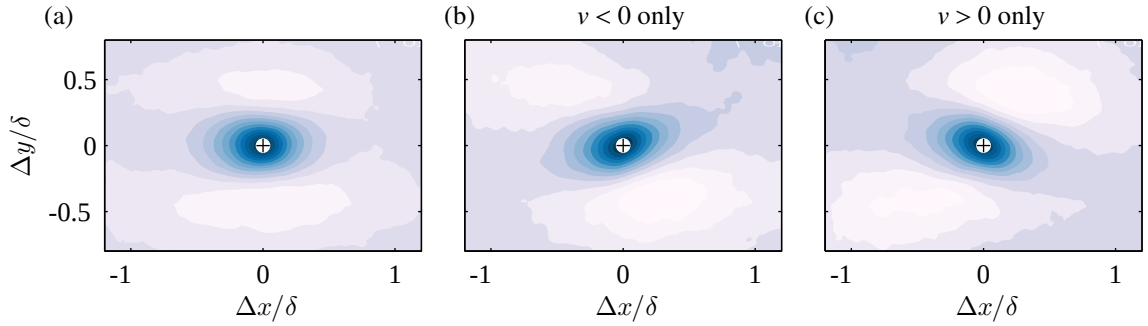

Figure 6: Conditional-averaged maps of kinetic energy $\langle K \rangle / (U_\infty^2/2)$ on a logarithmic scale. Results are presented on a xy plane at $z/\delta \approx 1$. (a) All turbulent bulges included; (b,c) when the bulge yield negative or positive spanwise velocity on average. Colour levels are the same as figure 5.

a pronounced tendency, which also concurs with observations from figure 1. However, the remaining characteristically squarish shape closer to the wall suggests that a superposition between two diagonals may still be present. In any case, it is evident that the oblique arrangement of the spanwise velocity appears clearer further away from the wall. Further, if one only includes the strongest v fluctuations the diagonal pattern has an increasingly stronger signature on R_{vv}.

Encouraged by the fact that spanwise velocity regions exhibit strong oblique behaviour, we suspect that turbulent bulges (Robinson, 1991) and the corresponding turbulent/non-turbulent interface TNTI (Corrsin & Kistler, 1955) may also display a tendency to be obliquely aligned from the main flow direction. First to detect the TNTI we employ a kinetic energy threshold, which has been shown previously to be well-suited to spatially locate the TNTI from PIV databases (see Chauhan *et al.* (2014); de Silva *et al.* (2013*b*)). In order to associate the non-turbulent outer region with zero kinetic energy, we compute the kinetic energy in a frame moving with the free-stream, i.e. the defect kinetic energy and is defined according to

$$K = \frac{1}{2}\left[(\widetilde{U} - U_\infty)^2 + \widetilde{V}^2\right]. \tag{3}$$

Figure 5 shows a sample PIV image and the interface determined based on the local defect kinetic energy, K, using a threshold of $K_0 = 10^{-3}\left(\frac{1}{2}U_\infty^2\right)$. This threshold yields an interface that agrees very well with the location where turbulent and the non-turbulent flow are visually observed to separate. Next, we examine conditionally averaged statistical properties in the near vicinity of these turbulent bulges. To perform this, a frame of reference attached to the centroid of each region is employed as the conditioning point (i.e. the location at which $\Delta x, \Delta y = 0$). Figure 6(a) represents the average kinetic-energy in the near-vicinity of the detected turbulent bulges at $z/\delta \approx 1$ (i.e about their centroids in figure 5). In figure 6(b,c) however, we include only regions where the average spanwise velocity within each bulge is either negative or positive. These results indicate that the orientation of turbulent bulges is indeed affected by the oblique coherence of v, and the streamwise-aligned representation shown in figure 6(a) is a superposition between equally frequent yawed turbulent bulges. Although not reproduced here, we note that these yawed bulges can also be observed three-dimensionally from the numerical databases of de Silva *et al.* (2013*a*).

Attached Eddy model

Based on our observations for the coherence in v, and inspired by the attached eddy hypothesis (Townsend, 1976), here we test if Λ-shaped eddies, which essentially are pairs of inclined vortices, distributed randomly in the plane of the wall can produce similar behaviour for the coherence of v. To construct the synthetic velocity fields, a packet of hairpin vortices is used as a representative eddy. Here, the representative eddy captures the bulk features of the average eddy shape, and we have chosen a representative eddy similar to that described in Marusic (2001), where multiple eddies are aligned in the streamwise direction to form packets (see also recent works by Baidya *et al.* (2014); Woodcock & Marusic (2015); de Silva *et al.* (2016). More extensive details on the computational process to generate the synthetic databases and scaling of the velocity fields can be found in de Silva *et al.* (2016).

A wall-parallel slice of one such synthetic velocity field of spanwise velocity fluctuations, v, is shown in figure 7. The results are presented at a Reynolds number and wall height that are comparable to the experimental velocity field shown in figure 1. Qualitatively, the synthetic and experimental velocity fields appear to be somewhat comparable. One notable difference is the lack of small scale activity in the model as it comprises only of wall-attached eddies whose growth is set by a geometric progression based on the distance from the wall. Nevertheless, the oblique pattern of v appears to be present from the model. Therefore, the model might provide some clues to the apparent obliqueness in v. However, further refinement of the representative structures in the model would be necessary in order to better capture the instantaneous flow features. For example, the present model only guarantees the preferential oblique alignment of pairs of positive and negative v regions, however, the experiments appear to visually exhibit v coherence for much longer extents (see figure 1).

Conclusions and outlook

This paper examines the large-scale oblique spatial organisation of the spanwise velocity component in turbulent boundary layers. To this end, a set of multi-camera PIV measurements are described to capture a sufficiently large spatial domain in excess of ten times the boundary layer thickness. Targeted inspections in the wake region using quantitative measures of correlation functions have shown a strong preferential alignment at $\pm 45°$, based on the sign of the spanwise velocity. The alignment also appears to be more discernible with increasing wall-normal location. Further, we observe that the oblique spatial arrangement appears to coincide with the organisation of the intermittent turbulent bulges, which leads to a pronounced impact on the geometry of the turbulent/non-

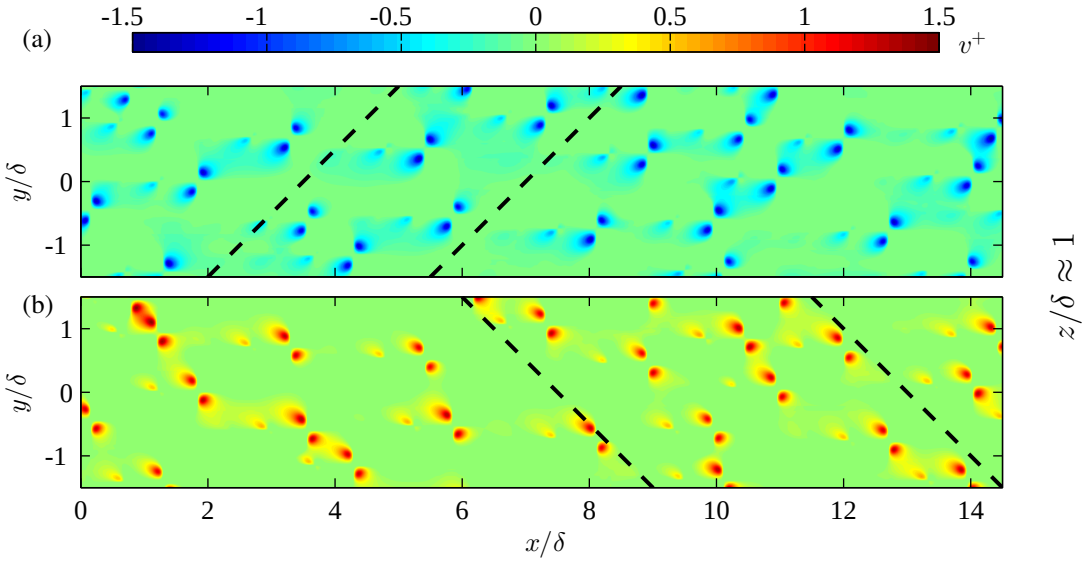

Figure 7: Instantaneous streamwise/spanwise plane of v from a AEM velocity field in the wake region of a boundary layer. (a) $v < 0$ and (b) $v > 0$. The black dashed lines correspond to ±45°.

turbulent interface.

To compliment the experimental observations from this study, synthetic datasets are generated by following the attached eddy models described in Marusic (2001), where the boundary layer is conceived as a collection of randomly located hairpin packets. These synthetic datasets are shown to generate an oblique spatial arrangement for coherent regions of v similar to those observed from experiments. Hence, these results indicate that the structures that underpin the oblique spanwise velocity coherence might have length-scale distributions similar to those described in the attached eddy work of Perry and co-workers.

REFERENCES

Adrian, R. J. & Westerweel, J. 2011 *Particle Image Velcimetry*. Cambridge University Press.

Baidya, R., Philip, J., Monty, J. P., Hutchins, N. & Marusic, I. 2014 Comparisons of turbulence stresses from experiments against the attached eddy hypothesis in boundary layers. In *Proc. 19th Aust. Fluid Mech. Conf.*.

Chauhan, K., Philip, J., de Silva, C. M., Hutchins, N. & Marusic, I. 2014 The turbulent/non-turbulent interface and entrainment in a boundary layer. *J. Fluid Mech.* **742**, 119–151.

Corrsin, S. & Kistler, A. L. 1955 Free-stream boundaries of turbulent flows. *NACA Tech. Note* p. 1244.

Grayson, K., **C. M. de Silva**, Hutchins, N. & Marusic, I. 2016 Laser light sheet profile and alignment effects on piv performance. In 18^{th} *Int. Symp. on App. Laser Tech. Fluid Mech., Lisbon, Portugal*.

Herpin, S., Stanislas, M., Foucaut, J. M. & Coudert, S. 2013 Influence of the Reynolds number on the vortical structures in the logarithmic region of turbulent boundary layers. *J. Fluid Mech.* **716**, 5–50.

Hutchins, N. & Marusic, I. 2007 Evidence of very long meandering features in the logarithmic region of turbulent boundary layers. *J. Fluid Mech* **579**, 1–28.

Lee, J. H., Kevin, Monty, J. P. & Hutchins, N. 2016 Validating under-resolved turbulence intensities for PIV experiments in canonical wall-bounded turbulence. *Exp. Fluids* **57** (8), 129.

Marusic, I. 2001 On the role of large-scale structures in wall turbulence. *Phys. Fluids* **13**, 735.

Marusic, I. & Adrian, R. J. 2012 The eddies and scales of wall turbulence. In *Ten Chapters in Turbulence*. Cambridge University Press.

Nickels, T. B., Marusic, I., Hafez, S. & Chong, M. S. 2005 Evidence of the k^{-1} law in a High-Reynolds-Number Turbulent Boundary Layer. *Phy. Rev. Lett.* **95** (7), 074501.

Robinson, S. K. 1991 Coherent motions in the turbulent boundary layer. *Ann. Rev. Fluid Mech.* **23** (1), 601–639.

Scarano, F. 2001 Iterative image deformation methods in PIV. *Meas Sci Tech.* **13**, R1–19.

Sillero, J. A., Jiménez, J. & Moser, R. D. 2013 One-point statistics for turbulent wall-bounded flows at Reynolds numbers up to $\delta^+ = 2000$. *Phys. Fluids* **25** (10), 105102.

Sillero, J. A., Jiménez, J. & Moser, R. D. 2014 Two-point statistics for turbulent boundary layers and channels at Reynolds numbers up to $\delta^+ = 2000$. *Phys. Fluids* **26** (10), 105109.

de Silva, C. M., Atkinson, C., Buchmann, N. A., Gnanamanickam, E.P., Hutchins, N., Soria, J. & Marusic, I. 2013*a* Nested multi-resolution PIV measurements of wall bounded turbulence at high Reynolds numbers. 10^{th} Int. Symp. Part. Im. Vel.

de Silva, C. M., Gnanamanickam, E.P., Atkinson, C., Buchmann, N. A., Hutchins, N., Soria, J. & Marusic, I. 2014 High spatial range velocity measurements in a high Reynolds number turbulent boundary layer. *Phys. Fluids* **26** (2), 025117.

de Silva, C. M., Hutchins, N. & Marusic, I. 2016 Uniform momentum zones in turbulent boundary layers. *J. Fluid Mech.* **786**, 309–331.

de Silva, C. M., Philip, J., Chauhan, K., Meneveau, C. & Marusic, I. 2013*b* Multiscale geometry and scaling of the Turbulent-Nonturbulent Interface in high Reynolds number boundary layers. *Phys. Rev. Lett.* **111**, 044501.

Townsend, A. A. 1976 *The structure of turbulent shear flow*, 2nd edn. Cambridge University Press.

Westerweel, J. 1997 Fundamentals of digital particle image velocimetry. *Meas Sci Tech.* **8**, 1379–1392.

Westerweel, J., Elsinga, G. E. & Adrian, R. J. 2013 Particle image velocimetry for complex and turbulent flows. *Ann. Rev. Fluid Mech.* **45**, 409–436.

Woodcock, J. D. & Marusic, I. 2015 The statistical behaviour of attached eddies. *Phys. Fluids* **27** (1), 015104.